A tunable photonic crystal filter for terahertz frequency applications

Timothy D. Drysdale[a], Richard J. Blaikie[b], David R.S. Cumming[a]

[a]Department of Electronics & Electrical Engineering, University of Glasgow, Glasgow G12 8LT, United Kingdom
[b]MacDiarmid Institute for Advanced Materials and Nanotechnology, Department of Electrical & Computer Engineering, University of Canterbury, Private Bag 4800, Christchurch, New Zealand

ABSTRACT

In this Paper we investigate a tunable metallic photonic crystal filter with a novel mechanical tuning method, suitable for use in terahertz frequency applications. Tuning has been demonstrated in a micrometer-driven prototype at 70 – 110 GHz in accordance with rigorous full-vector electromagnetic simulations (finite-difference time-domain). The measured pass band has a Q of 11 and can be tuned over a 3.5 GHz range. The insertion loss is only 1.1 to 1.7 dB, while the stop band attenuation is >10 dB. The filter has the advantages of inexpensive, robust and compact construction and tunable operation that readily scales to any desired terahertz frequency.

Keywords: metallic photonic crystal, photonic band gap, capacitive coupling, tunable filter, microwave, terahertz

1. INTRODUCTION

Many emerging terahertz applications require tunable frequency discrimination. Examples of where such ability is essential are in spectroscopy for chemical and biological sensing, and in frequency division multiplexing schemes for terahertz communications within secure pico-cell networks or between satellites. While technologies have been developed for the infrared[1, 2] and visible[3] regions, they may be difficult to fabricate for the longer terahertz wavelengths. Furthermore, devices constructed from lossy substrates may be unsuitable for the expected microwatt power levels.[4] Hence, new methods are required in order to take advantage of broadband sources and detectors in these applications.

Metallic photonic crystal filters are a promising alternative because they are compact, robust and inexpensive. Photonic crystals are periodic structures that exhibit characteristic gaps in their electromagnetic dispersion relation. In other words, when illuminated by an electromagnetic wave these structures give rise to multiple internal reflections that constructively or destructively interfere depending on the wavelength. In this way, there are bands of frequencies (photonic band gaps or stop bands) for which the interference is destructive and propagation through the crystal is prohibited. Furthermore, one or more narrow pass pass bands may be introduced into the stop band by creating a defect in the structure, such as a missing rod or an extra air layer. Hence photonic crystals make useful filters, however the few tuning schemes that are known may not be suitable in all applications.[5, 6] In this paper, we demonstrate a novel mechanical tuning mechanism for metallic photonic crystal filters.

Further author information: (Send correspondence to D.R.S.C.)
T.D.D.: E-mail: t.drysdale@elec.gla.ac.uk
R.J.B.: E-mail: blaikie@elec.canterbury.ac.nz
D.R.S.C.: E-mail: d.cumming@elec.gla.ac.uk, Telephone: +44 (0)141 330-5233, Fax: +44 (0)141 330 4907.

2. THEORY OF OPERATION

The basic component of the filter is a metal plate comprising two orthogonal linear metallic grids as shown in Fig. 1(a) (not to scale). Each plate is made from a single piece of metal and contains integral lugs with holes for mounting and actuation. Further mechanical support may be provided to the grids by extending the mounting lugs around all four sides of each plate (not shown). The filter is constructed by stacking two such plates to give the device cross section shown in Fig. 1(b) (lugs omitted). Linearly-polarized plane-waves are normally incident from above, with the electric field, **E**, oriented as shown (the orthogonal linear polarization is blocked). All the rods in the grids are of subwavelength size, having dimensions of width r, depth d, and period Λ. The inner two grids are initially aligned, and an allowance is made for a small fixed separation, g, between the plates.

The transmission characteristic of this device exhibits a plasmon-like forbidden band that extends from zero frequency up to a cut-off frequency, f_c, where the associated wavelength, λ_c, is approximately equal to the twice the lattice constant of the 3-D metallic grid structure[7] ($\lambda_c \approx 2\Lambda$). This behavior is analogous to the plasmonic behavior of a bulk metal, except that for a bulk metal the cut-off frequency (plasma frequency) is typically in the UV region. In the present device, the effective plasma frequency f_c is lowered from the UV to terahertz frequencies by the geometry of the plates.[8] This high-pass behavior may also be explained in terms of the capacitance and inductance of the grids.

There is a single-peaked transmission band located just above the cutoff frequency, associated with the single layer of micro-cavities formed in the center of the device.[9] If the number of plates was increased, the passband would split into several distinct peaks, with the number of peaks being equal to $(N-1)$ where N is the number of plates in device.[9] There may be multi-channel communications or multi-band spectroscopy applications in which multiple tunable peaks are advantageous, however these structures are not explored here. Most metals may be treated as perfect electrical conductors at microwave and terahertz frequencies,[10] hence the peak transmission is expected to be 0 dB.

The center frequency of the transmission peak is tuned by a relative lateral shift, $0 < s < \Lambda/2$, of the plates in a direction parallel to the inner grid's grating vector, **K**, as shown in Fig. 1(c). The plate separation g is not used to tune the device, and therefore the tuning method is different to Fabry-Pérot cavity-based techniques.[5,11] The position of the outer rods is not adjusted because it does not affect the tuning, although the supporting results are not presented here. For $s < r$ the rods of the inner grids overlap, and the strong capacitive coupling influences the frequency, f_p, of the transmission peak according to $f_p \approx \sqrt{LC}$ where L is the inductance and C the capacitance of the device.[12] As s increases, the overlapped area of the rods shrinks and the capacitive coupling reduces, lowering the peak frequency. Since the shifted structure has two-fold rotationally symmetry,

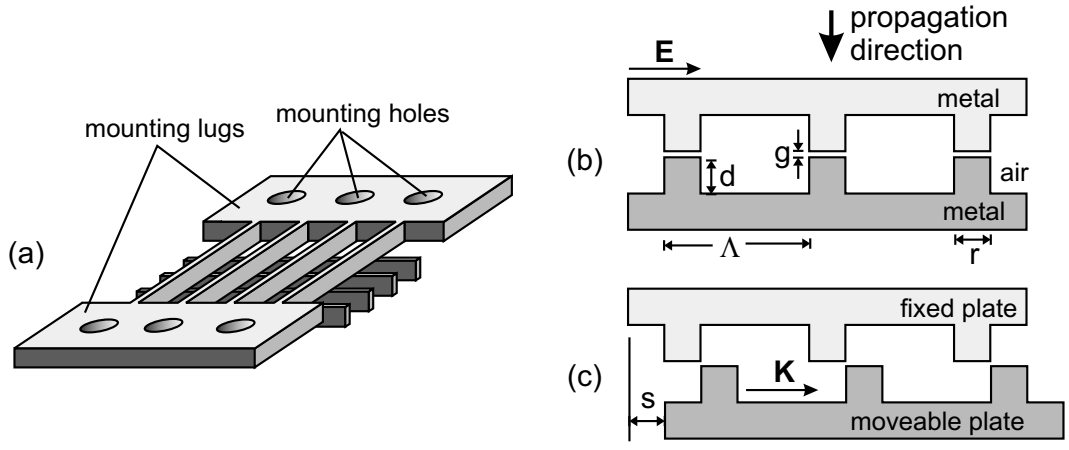

Figure 1. (a) One of two metal plates required to make the filter. Each plate is made from a single piece of metal. (b) The cross section through the device with two plates. (c) Tuning is achieved by lateral shifts s of one plate parallel to the inner grids' grating vector **K**. The plate separation g is not used to tune the device, and is ideally zero.

the maximum useful movement is a half period, $\Lambda/2 = 900\ \mu$m. For example, shifts of s and $(\Lambda - s)$ are equivalent in terms of the electromagnetic behavior of the structure.

Above the first transmission band lies the second (true) photonic band gap,[9] and into this gap there is introduced a defect mode resonance if there are any disturbances to the regular periodicity of the crystal. A defect mode resonance is expected for shift positions that result in asymmetric spacing of the inner grids ($s \neq 0, \Lambda/2$).

For operation in the W-band (70 – 110 GHz, $2.7 < \lambda_0 < 4.2$ mm), the following dimensions were chosen: $\Lambda = 1.8$mm, $r = 450\mu$m, $d = 500\mu$m. These dimensions can be adjusted to fine tune the filter properties or accommodate fabrication constraints, or scaled for operation at other microwave and terahertz frequencies. For example, if the thickness of the metal sheet was constrained to smaller value, then the period of the grids could be increased to maintain the same pass-band frequency range.

3. SIMULATION

The expected performance of a prototype was quantified using a Finite-Difference Time-Domain (FDTD) analysis method. A slightly modified version of the TEMPEST code was used, originally written at the University of California, Berkeley.[13] FDTD tracks the time varying fields in a volume of space by solving Maxwell's time dependent curl equations directly, over a finite volume that has been discretised into two interleaving grids, one representing the electric field ($\mathbf{E}$)and the other representing the magnetic field ($\mathbf{H}$):

$$\nabla \times \mathbf{E} = -\mu \frac{\partial \mathbf{H}}{\partial \mathbf{t}} \tag{1}$$

$$\nabla \times \mathbf{H} = \sigma \mathbf{E} + \epsilon \frac{\partial \mathbf{E}}{\partial \mathbf{t}}, \tag{2}$$

where t is time and ϵ, μ and σ are the position-dependent permittivity, permeability and conductivity, respectively.

To ensure accuracy and stability in the simulation, the spatial resolution of the grids must be better than about $\lambda/10$ (where λ is the shortest wavelength considered) and the time step Δt must be shorter than the time taken for a wave to propagate between any adjacent points:

$$\Delta t < \frac{\Delta x}{c} \tag{3}$$

As a consequence, the computational load is high. In order to achieve practical calculation times, advantage must be taken of any symmetries in the device in order to reduce the size of the volume over which the fields are calculated. In this case, an infinitely wide grid was modeled by surrounding a single unit cell of the device with periodic boundary conditions, as shown in Fig. 2 (not to scale). The top and bottom of the simulation domain were truncated with 12 cells of Berenger's Perfectly Matched Layer (PML) boundary condition in order to absorb the outgoing waves with reflection < -80 dB.[14] The total size of the simulation domain was 1.8 mm by 1.8 mm by 8.1 mm and comprised 60 by 60 by 270 cubic cells each measuring 30μm per side.

Gaussian-pulsed plane-wave excitation was used in order to allow the frequency response of the filter in a particular setting to be calculated in a single simulation. Using the principle of superposition, the response to both orthogonal linear polarizations was able to be calculated in the same simulation with no performance penalty. There is however a slight time penalty associated with saving the recorded field data to disk at each time step, in addition to a severe storage space penalty. In order to overcome these problems, the original TEMPEST code was modified to output the sum of the electric fields recorded in the plane of the electric field sensor. This resulted in a three-orders-of-magnitude reduction in the total amount of data that needed to be stored.

The simulation was terminated after a pre-determined number of time steps. The recorded electric fields were then post-processed with the fast Fourier transform (FFT) algorithm in order to provide the desired frequency response of the filter. The intermediate stages in the processing of the FDTD simulation results are shown in Fig. 3, with the time-varying electric fields as recorded during the simulation in Fig. 3(a) and the resulting FFT

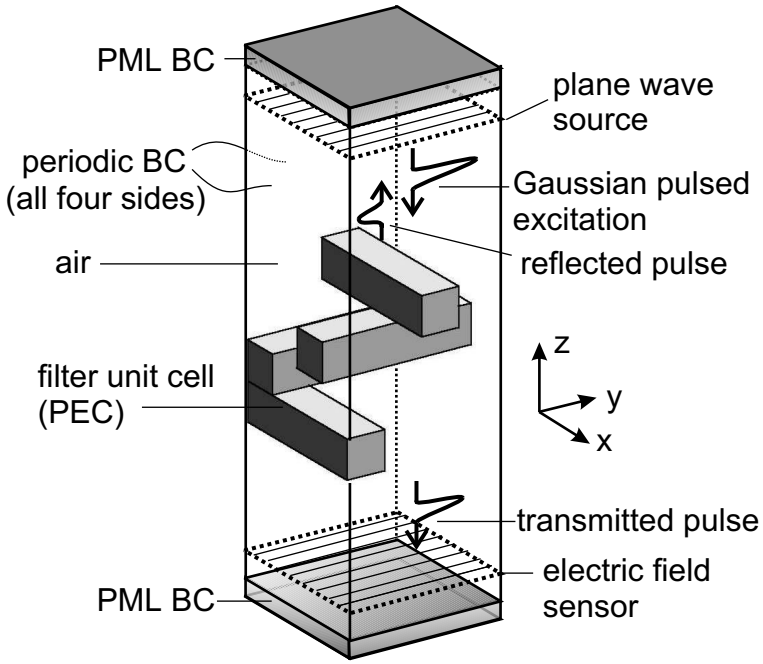

Figure 2. The Finite-Difference Time-Domain simulation domain employs periodic boundary conditions in order to model a device with a grid of infinite lateral extent with just a single unit cell.

frequency spectra in Fig. 3(b). Two sets of simulation data are shown in Fig. 3. The frequency response of the filter shown in Fig. 3(b) is weighted by the power spectral density of the incident wave and therefore does not give the transmission intensity directly. However, it may be de-embedded by dividing by the frequency response of the empty simulation domain (free space) under the same excitation conditions.

The frequency resolution of the FFT is determined by the step size, and the number of time steps, according to the following relation

$$\Delta f = \frac{1}{N\Delta t}, \tag{4}$$

where N is the number of time steps input to the FFT algorithm and Δt is the time step. For the present simulations, $\Delta t = 58$ fs and $N = 2^{15}$ yielding a frequency resolution of 0.53 GHz.

Each simulation ran for approximately 200 minutes on a 2 GHz Intel Pentium IV processor operating under Red Hat Linux version 7.1. Two different tuning positions ($s = 0, 240$ μm) were simulated. Note that in the simulations the plate separation was set to the minimum non-zero distance (one simulation cell), giving $g = 30$ μm.

4. MEASUREMENT

A prototype device with an area of 34 mm by 30 mm (excluding the lugs) was constructed from 1 mm thick 5251 aluminum alloy sheet using conventional computer numerical control (CNC) milling techniques. Due to the large dimensional tolerances associated with conventional machining techniques, the rod widths varied from $260 < r < 480$ μm, but the period and depth were regular and none of the rods were broken. Burrs left by the machining processes were cleaned away using a scalpel with the aid of a stereographic microscope. For extra mechanical support of the grid, the plate was designed with lugs that extended all the way around, giving a total plate size of 60 mm by 40 mm. Three mounting holes of 3 mm diameter were drilled at each end of the plate for mounting purposes. A photograph of the plate is presented in Fig. 4.

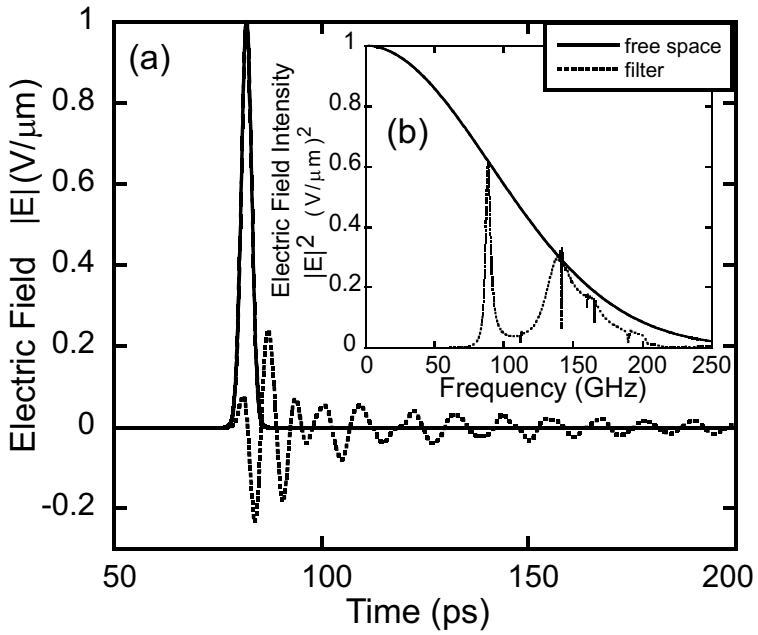

Figure 3. Intermediate steps in the processing of the Finite-Difference Time-Domain simulation data. (a) Recorded time-varying fields. (b) Frequency spectra obtained by discrete Fourier transform.

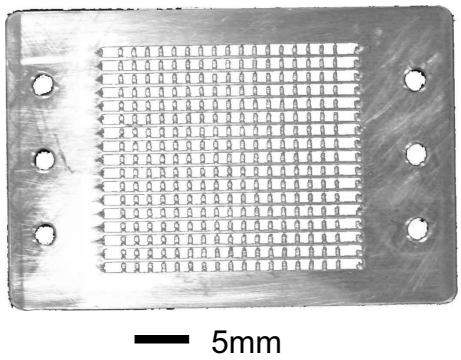

Figure 4. Photograph of one of the two identical aluminum plates that comprise the filter.

The plates were mounted on Tufnel holders having 34 mm × 34 mm apertures in the region of the grid and sandwiched between 20 mm × 20 mm square apertures of absorbing foam. The plates were actuated by a three-axis translation stage and differential micrometers. Stray reflections were eliminated by covering nearby surfaces with absorbing foam. Full 2-port complex S-parameter measurements were taken using a Wiltron 360B vector network analyzer along with two WR-10 standard gain horn antenna, Wiltron SM4873 transmission-reflection measurement units and a Wiltron 61878B sweep synthesizer. After mixing in the transmission-reflection units, the power output was -15 dBm at 67 – 110 GHz. Separately, the self-extinction ratio of the horn antenna was measured to be > 32 dB, indicating that the horn antenna output was sufficiently linearly polarized for the present purposes.

The experimental setup is illustrated in Fig. 5, with a schematic of the equipment connections in Fig. 5(a) and a photograph showing the device and mounting apparatus in relation to the horn antennas in Fig. 5(b). Note that in Fig. 5(b) some of the absorbing foam has been removed from the apparatus for photographic purposes.

The measurement system was calibrated without the horn antenna, according to the line-reflect-line method, using a Flann Microwave bronze WR-10 calibration kit. The calibration kit comprised a through-waveguide section, a flush short and a quarter-wavelength offset. The through-waveguide section remained in the system after calibration and is visible on the transmission-reflection unit on the right hand side of Fig. 5(b). The phase reference planes were located at the flanges of the test ports to which the horn antennas were connected. The calibration corrections were automatically applied by the the vector network analyzer to the measured S-parameter data before it was transferred over a GPIB bus to a PC where it was saved for later analysis.

Since the horn antenna were not included in calibration, an additional measurement was required to compensate for the losses in the free-space section of the measurement setup. After calibration, the horns were added and allowed to thermally stabilize for approximately 30 minutes before a reference measurement was taken of the entire experimental setup including a dummy filter with the gridded area missing. The loss in the dummy setup varied between -7 dB at 67 GHz to -10 dB at 110 GHz, due to the wider beam width at higher frequencies.

Fabry-Pérot resonances arising from multiple reflections between the horns and the device were averaged out by taking 15 measurements at different horn spacings in the range of 60 – 65 mm. An example of the result of this technique is presented in Fig 6, which shows the 15 individual measurements as thin dotted lines and the

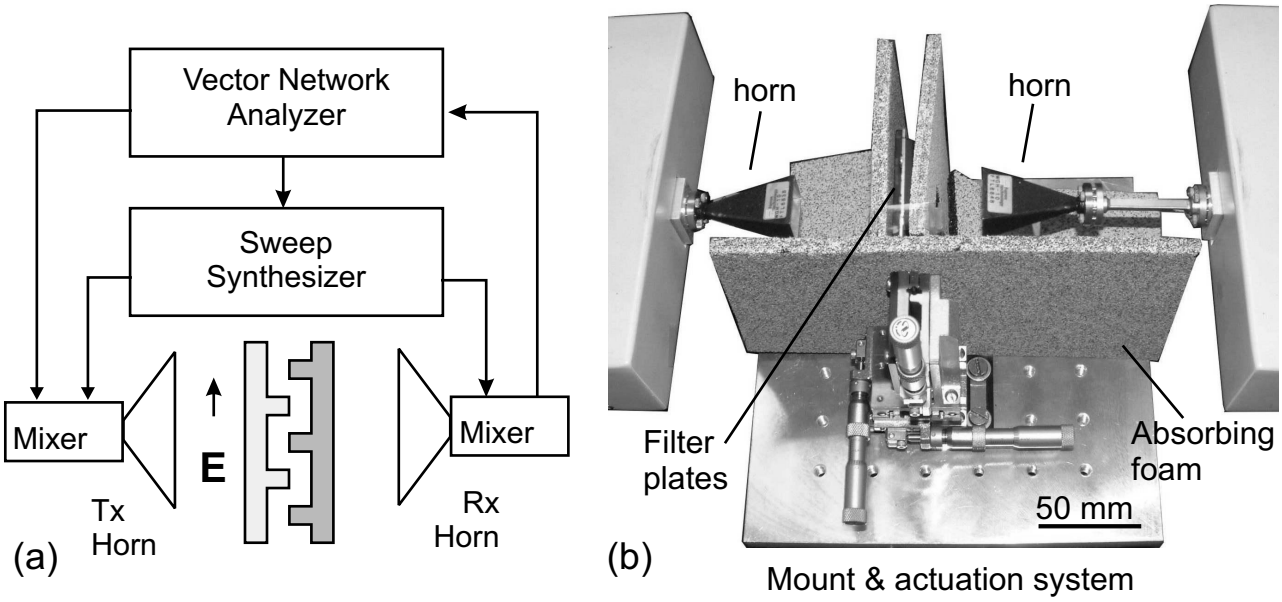

Figure 5. Experimental device and equipment setup. (a) Schematic of equipment connections. (b) Photograph of the mounting and actuation equipment and the horn antenna.

overall average as a thick solid line. Only the tip of the peak is shown because the Fabry-Pérot resonances are much smaller than the main features.

During measurements, the two plates were brought into intimate contact with slight pressure in order to minimize the separation g. This did not damage the grids because each plate was supported on all sides by mounting lugs. Despite these precautions, some inhomogeneity in the plate separation was observed, with g typically 10 μm. The plates were drawn apart by 300 μm between each lateral shift in order to ensure that the lateral shifts were performed accurately. Future implementations of the device, other than this initial proof-of-concept prototype, would not necessarily require this precaution and thus single-axis actuation would suffice. The device was measured at each of the tuning positions for which simulations were performed.

5. SIMULATION AND EXPERIMENTAL RESULTS

The transmission characteristics of the filter are plotted in Fig. 7 for the tuning positions $s = 0, 240$ μm, with simulated results in Fig. 7(a) and measured results in Fig. 7(b). Examining Fig. 7(a), the transmission peak t_1 shows tuning over a 4.7 GHz range for a shift of $s = 240$ μm, giving a tuning sensitivity of 20 GHz/mm. The maximum predicted transmission of peak t_1 is -0.1 dB, with 0 dB not being observed due to the frequency resolution of the FFT, while the defect mode resonance t_2 is predicted to peak at -2.1 dB. The quality factor (Q) of the peaks varies from 21 – 27 for t_1 and is 93 for t_2. The measured device performs similarly, with measured peaks m_1 and m_2 corresponding to the simulated peaks t_1 and t_2. The tuning range shown by peak m_1 is lower than predicted, at 3.5 GHz, giving a tuning sensitivity of 15 GHz / mm. This peak is slightly lossier than predicted, with the loss varying from -1.1 to -1.7 dB, while the defect mode resonance peak is at -7.4 dB. The loss is attributed to the finite conductivity of the plates, although there may also be a contribution from a systematic error in de-embedding the loss of the free-space measurement setup. The stop band attenuation is

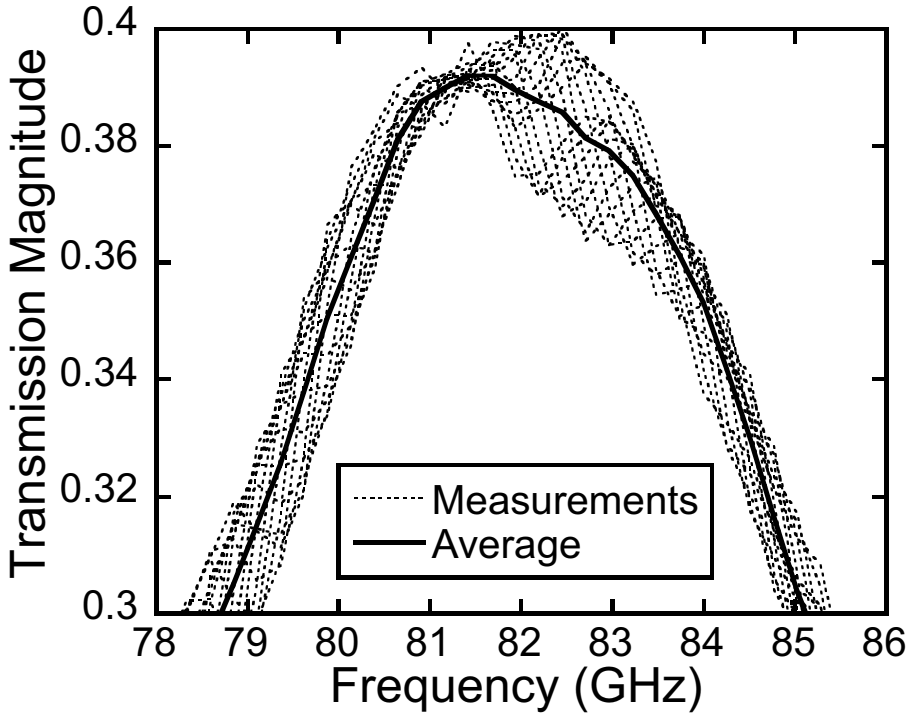

Figure 6. Example of the spatial averaging technique that eliminates the Fabry-Pérot resonances arising from multiple reflections between the horn antenna and the filter. Fifteen sets of measurements are plotted as dotted lines, while the solid line is their average. The peak shows significantly less than 100% transmission because the loss of the test set has not yet been de-embedded.

>10 dB, in good agreement with the simulations. The Q of the measured peaks is also lower at 11 and 17 for peaks m_1 and m_2 respectively. Peaks m_1 and m_2 are located approximately 7 GHz lower than t_1 and t_2. The reduced tuning range and Q observed in the measurements is attributed to non-zero separation g between the plates, the variation in the fabricated rod width,[15] and the $\sim 6^\circ$ range of incident angles arising from the use of standard-gain horn antenna.

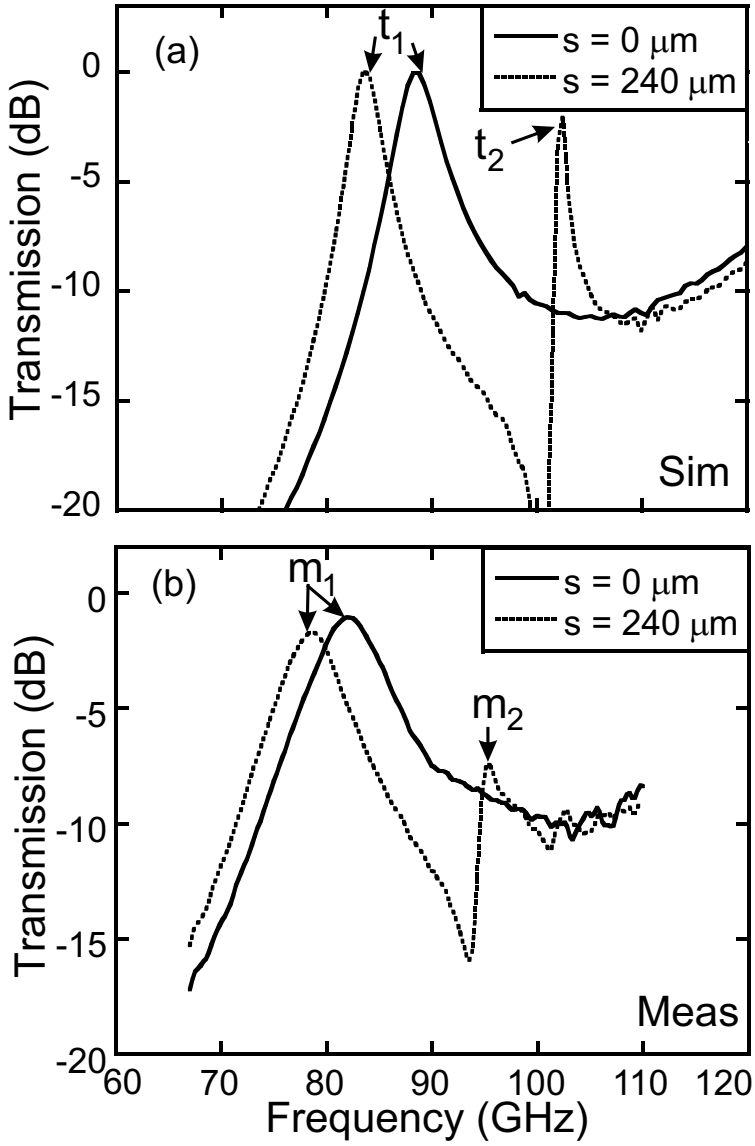

Figure 7. Frequency spectra of the filter prototype at the tuning positions $s = 0, 240$ μm. (a) Simulated, (b) measured.

6. CONCLUSION

A metallic photonic crystal filter with a novel mechanical tuning method has been investigated. The tuning of a single-peaked transmission pass band is accomplished by a relative lateral shift of the two gridded plates that comprise the filter. Tuning was demonstrated in a prototype device at 70 – 110 GHz in accordance with finite-difference time-domain simulations. The measured device exhibited a pass band Q of 11 and a tuning range of 3.5 GHz. The insertion loss was 1.1 to 1.7 dB, slightly lower than the expected 0 dB due to the finite conductivity of the aluminum from which the plates were fabricated. The prototype was fabricated using conventional milling processes, yielding a device that is straightforward and inexpensive to produce and robust, compact and tunable in operation.

ACKNOWLEDGMENTS

This work is funded by Scottish Enterprise's Proof of Concept fund.

REFERENCES

1. H. Alause, J. Malzoc, F. Grasdepot, V. Nouaze, J. Hermann, and W. Knap, "Micromachined optical tunable filter for long term gas stability sensors," *IEE Proc. Optoelectronics* **144**, October 1997.
2. G. Lammel, S. Schweizer, S. Schiesser, and P. Renaud, "Tunable optical filter of porous silicon as key component for a MEMS spectrometer," *J. Microelectromech. Syst.* **11**, Dec 2002.
3. P. Bondavalli, R. LeDantec, and T. Benyattou, "Influence of the involuntary underetching on the mechanical properties of tunable Fabry-Pérot filters for optical communications," *J. Microelectromech. Syst.* **10**(2), 2001.
4. P. Siegel, "Terahertz technology," *IEEE Trans. Microwave Theory Tech.* **50**, pp. 910 – 928, March 2002.
5. B. Temelkuran, H. Altug, and E. Ozbay, "Experimental investigation of layer-by-layer metallic photonic crystals," *IEE Proc. Optoelectronics* **145**(6), pp. 409 – 414, 1998.
6. J.-M. Lourtioz, A. de Lustrac, F. Gadot, A. Chelnokov, T. Brillat, A. Ammouche, J. Danglot, O. Vanbésien, and D. Lippens, "Toward controllable photonic crystals for centimeter and millimeter-wave devices," *J. Lightwave Tech.* **17**, pp. 2025 – 2031, November 1999.
7. D. Sievenpiper, M. Sickmiller, and E. Yablonovitch, "3D wire mesh photonic crystals," *Phys. Rev. Lett.* **76**(14), pp. 2480 – 2483, 1996.
8. J. Pendry, A. Holden, W. Stewart, and I. Youngs, "Extremely low frequency plasmons in metallic mesostructures," *Phys. Rev. Lett.* **76**, pp. 4773 – 4776, June 1996.
9. F. Gadot, A. de Lustrac, J.-M. Lourtioz, T. Brillat, A. Ammouche, and E. Akmansoy, "High-transmission defect modes in two-dimensional metallic photonic crystals," *J. Appl. Phys.* **85**, pp. 8499 – 8501, June 1999.
10. S. Fan, P. Villeneuve, and J. D. Joannopoulos, "Large omni-directional band gaps in metallodielectric photonic crystals," *Phys. Rev. B* **54**, pp. 11 245 – 11251, October 1996.
11. R. Ulrich, T. J. Bridges, and M. A. Pollack, "Variable metal mesh coupler for far infrared lasers," *Appl. Opt.* **9**, pp. 2511 – 2516, November 1970.
12. D. Sievenpiper, E. Yablonovitch, J. Winn, S. Fan, P. Villenueve, and J. Joannopoulos, "3D metallo-dielectric photonic crystals with strong capacitive coupling between metallic islands," *Phys. Rev. Lett.* **80**(13), pp. 2829 –2832, 1998.
13. T. V. Pistor, K. Adam, and A. Neureuther, "Rigorous simulation of mask corner effects in extreme ultraviolet lithography," *J. Vac. Sci. Tech. B* **16**, pp. 3449–3455, Nov 1998.
14. A. Taflove and S. C. Hagness, *Computational Electrodynamics: the finite difference time domain method*, p. 314. Artech House, Boston, second ed., 2000.
15. J. McCalmont, M. Sigalas, G. Tuttle, K.-M. Ho, and C. Soukolis, "A layer-by-layer metallic photonic band-gap structure," *Appl. Phys. Lett.* **68**, pp. 2759 – 2761, May 1996.